

Kernel based quantum machine learning at record rate: Many-body distribution functionals as compact representations

Danish Khan,^{1,2} Stefan Heinen,² and O. Anatole von Lilienfeld^{2,3,4,*}

¹*Department of Chemistry, University of Toronto, St. George Campus, Toronto, ON, Canada*

²*Vector Institute for Artificial Intelligence, Toronto, ON, M5S 1M1, Canada*

³*Departments of Chemistry, Materials Science and Engineering, and Physics,
University of Toronto, St. George Campus, Toronto, ON, Canada*

⁴*Machine Learning Group, Technische Universität Berlin and Institute
for the Foundations of Learning and Data, 10587 Berlin, Germany*

The feature vector mapping used to represent chemical systems is a key factor governing the superior data-efficiency of kernel based quantum machine learning (QML) models applicable throughout chemical compound space. Unfortunately, the most accurate representations require a high dimensional feature mapping, thereby imposing a considerable computational burden on model training and use. We introduce compact yet accurate, linear scaling QML representations based on atomic Gaussian many-body distribution functionals (MBDF), and their derivatives. Weighted density functions (DF) of MBDF values are used as global representations which are constant in size, i.e. invariant with respect to the number of atoms. We report predictive performance and training data efficiency that is competitive with state of the art for two diverse datasets of organic molecules, QM9 and QMugs. Generalization capability has been investigated for atomization energies, HOMO-LUMO eigenvalues and gap, internal energies at 0 K, zero point vibrational energies, dipole moment norm, static isotropic polarizability, and heat capacity as encoded in QM9. MBDF based QM9 performance lowers the optimal Pareto front spanned between sampling and training cost to compute node minutes, effectively sampling chemical compound space with chemical accuracy at a sampling rate of ~ 48 molecules per core second.

I. INTRODUCTION

Modern data-driven statistical Machine Learning (ML) models have emerged as powerful tools over the past decade for inferring quantum mechanical observables throughout chemical compound space, without explicitly solving electronic Schrödinger equations¹⁻³. Similar success was obtained for ML based interatomic potentials and force-fields⁴⁻⁹ as well as electronic structure modeling throughout Chemical Compound Space (CCS)^{10,11}. For an entire set of extensive in-depth reviews on these and other related ML applications, we refer the reader to the recent special issue in Chemical Reviews^{12,13}. Various aspects in the development of ML model architecture and training protocols have proven to be essential for data-efficiency. In particular, the molecular representation is known to have a strong impact on the performance of similarity based ML models, such as kernel ridge regression (KRR)¹⁴⁻¹⁶. This is not surprising as the representation controls the information about the systems, how its weighed and the consistency of these Quantum Machine Learning (QML) models with *ab-initio* methods¹⁷. These representations are non-linear mappings of the atomistic systems to a suitable Hilbert Space where a statistical regression model can easily be applied. The Hilbert Space constraint applies due to the requirement of measuring similarity in terms of an inner product¹⁸. These mappings should have

some desirable features of which the most important are i) uniqueness such that systems with different properties necessarily possess different representations¹⁴ and ii) invariance with respect to transformations that leave the target property invariant, such as global translations, rotations, and atomic index permutations of the same chemical elements. Other desirable features include iii) an analytical and continuous form of the representation function, iv) differentiability with respect to nuclear coordinates, charges, number of electrons, and number of atoms, v) as general as the Hamiltonian, vi) computationally efficient evaluation, vii) compact or even constant size, limiting the computational cost for larger systems¹⁹.

Due to their critical role, many representations have been introduced and investigated within the context of atomistic simulation²⁰⁻³². For recent comprehensive reviews, the reader is referred to Refs. 16,33. These representations can either describe the molecule as a whole (global) or each atom (local or atomic) separately. For the sake of brevity we restricted most of our comparative benchmarks within this study to the following representations which are commonly used to train QML models throughout CCS: Faber-Christensen-Huang-Lilienfeld (FCHL19) representation^{34,35}, Smooth Overlap of Atomic Positions (SOAP)³⁶, spectrum of London and Axilrod-Teller-Muto potentials (SLATM)³⁷, atom index sorted Coulomb matrix (CM)¹, and its vectorized form, Bag of Bonds (BOB)³⁸. Other representations/models tested are mentioned in the data and code section.

While these representations satisfy most of the aforementioned qualities, seen the immense size of CCS, a

* anatole.vonlilienfeld@utoronto.ca

more compact and scalable representation would still be desirable. Formally, the number of degrees of freedom of any material or molecule would prescribe usage of a $4M$ dimensional feature vector (3 spatial coordinates and one nuclear charge coordinate for each of the atoms). However, all aforementioned representations when using optimal hyperparameters require a higher dimensional feature vector mapping in order to be accurate and training-data-efficient at regression tasks, and some (e.g. CM or BOB) even scale quadratically with M . While verbosity facilitates the inclusion of invariances, the $4M$ degrees of freedom suggest that the same performance can be obtained using more compact representations. This is especially an issue for kernel based ML models, where the size of the representation directly affects the distance/kernel evaluation time^{18,34}. Although the scaling for kernel inversion³⁹ is larger ($\propto \mathcal{O}(n^3)$ for Cholesky solvers), for highly data-efficient (i.e. efficient in training data) QML models it is the kernel generation and evaluation that consumes the most compute time as demonstrated later. The kernel evaluation pre-factor becomes even worse when using atomic (or local) representations in conjunction with a suitable local kernel⁴⁰. Obvious solutions by reducing finite local cutoffs within the representation come at the expense of reducing the predictive power, or, conversely, increasing training data needs. As such, a computationally efficient yet accurate solution is desirable as was shown in the discretization of the FCHL18 representation^{34,35}. Other solutions to this problem such as sparse kernel models⁴¹ and the recently introduced conjugate gradients based iterative approach for training kernel based models⁴² would also be well complemented by a compact molecular representation.

Herein, we propose a methodology for generating representations that minimize feature size. We use functionals of many-body distributions (MBDFs) and their derivatives to encode any local chemical environment of any atom in an integrated compact fashion. The representations thus generated preserve the system’s various symmetries (translation, rotation, atom index invariance), and can be tailored to the physical property of interest through scaling functions. MBDFs are easily extendable to include higher order many-body interactions with minimal increase in size. In the current formulation, while including three-body interactions, MBDF scales as $5M$. We further tackle the issue of storing this information in a manner that remains invariant to the number of atoms in a molecule. We do this by generating a discretized density (DF) function of MBDF values, and using it as a global molecular representation. Using two diverse datasets the performance of MBDF is tested against aforementioned SOAP and FCHL19, which are commonly used and state-of-the-art, as well as SLATM, BOB, CM representations and a few other QML models mentioned later. Lastly, we explore the bottleneck cross-over from kernel evaluation to inversion.

II. THEORY AND DISCUSSION

A. Many-Body Distribution Functionals

We begin the discussion of our local representation using distribution functions over the internal coordinates which can be constructed using the atomic coordinates.

An analytical and continuous distribution over the pair-wise internal coordinate defined as the inter-atomic distances (pair correlation function), is easily built using Gaussian probability density functions (PDFs) centered at each inter-atomic distance with respect to an atom i :

$$\rho_i(r, R_{ij}) = \frac{1}{\sqrt{2\pi\sigma_r^2}} \sum_{j \neq i}^M Z_j \exp\left(-\frac{(r - R_{ij})^2}{\sigma_r}\right) \quad (1)$$

where $\rho_i(r, R_{ij})$ is the normalized distribution with atom i as the origin, σ_r is the Gaussian length-scale (or variance) parameter, M denotes the total number of atoms in the system (or within a radial cutoff if employed), R_{ij} denotes the inter-atomic distance between atoms i and j and Z_j is the nuclear charge. Scaling by nuclear charges defines elemental identities, but could also be done in other ways e.g. having different length-scale parameters σ_r for each unique chemical element, or multiple dimensions such as period and group specifications⁴³. In a similar fashion, a continuous distribution (triplet correlation function) over the 3-body internal coordinate, inter-atomic angles θ , is defined as:

$$\rho_i(\theta, \theta_{jik}) = \frac{1}{\sqrt{2\pi\sigma_\theta^2}} \sum_{j \neq i}^M \sum_{k \neq j}^M Z_j Z_k \exp\left(-\frac{(\theta - \theta_{jik})^2}{\sigma_\theta}\right),$$

$$\theta_{jik} = \cos^{-1} \frac{(\mathbf{R}_i - \mathbf{R}_j)^T (\mathbf{R}_i - \mathbf{R}_k)}{R_{ij}^2} \quad (2)$$

where θ_{jik} is the inter-atomic angle centered on atom i . This can be generalized to define a continuous distribution, or correlation function, over any m -body internal coordinate τ .

Such analytical distribution functions of the internal coordinates have been used as descriptors of atomic environments in Atom Centered Symmetry Functions^{6,20} (ACSF), their weighted variants wACSFs²³ and other similar methods. Instead of using these distribution functions as atomic descriptors, we define the MBDF representation as functionals of these m -body distributions which leads to a more compact descriptor and allows inclusion of higher order terms with minimal change in size (a single scalar for each m -body term). With the 2- and 3-body distributions defined above, each atom can then be represented by the two zeroth-order functionals:

$$F_0^{(2)}[i] = \int_0^{r_c} dr g_0(r, R_{ij}) \rho_i(r, R_{ij}) \quad (3)$$

$$F_0^{(3)}[i] = \int_0^\pi d\theta g_0(\theta, R_{ij}, R_{jk}, R_{ik}) \rho_i(\theta, \theta_{jik}) \quad (4)$$

where r_c denotes the radial cut-off distance, and $g_0(r, R_{ij})$ and $g_0(\theta, R_{ij}, R_{jk}, R_{kj})$ denote 2- and 3-body weighting functions. Note that when the weighting functions $g_0(r, R_{ij})$ and $g_0(\theta, R_{ij}, R_{jk}, R_{kj})$ correspond to suitable 2 and 3-body potentials, the functionals $F_0^{(2)}$, $F_0^{(3)}$ become the average of the corresponding 2, 3-body inter-atomic interactions weighted by the pair and triplet correlation functions $\rho_i(r, R_{ij})$, $\rho_i(\theta, \theta_{jik})$, respectively. These functionals then form a coarse approximation to the average 2, 3-body interactions experienced by a chemical species. Furthermore, we exploit the advantage of using the infinitely differentiable Gaussian PDFs to define higher order functionals such as:

$$F_1^{(2)}[i] = \int_0^{r_c} dr g_1(r, R_{ij}) \frac{\partial \rho_i}{\partial r}(r, R_{ij}) \quad (5)$$

$$F_1^{(3)}[i] = \int_0^\pi d\theta g_1(\theta, R_{ij}, R_{jk}, R_{ik}) \frac{\partial \rho_i}{\partial \theta}(\theta, \theta_{jik}) \quad (6)$$

with potentially different weighting functions $g_1(r)$, $g_1(\theta, R_{ij}, R_{jk}, R_{kj})$. The derivative functionals are useful since the functional of any arbitrary distribution is not unique. These functionals also encode the change in the m -body distribution in an atom's local neighborhood and have not been used in previous works involving internal coordinate distribution functions. For any n -th derivative of the 2-body distribution we can define the functional:

$$F_n^{(2)}[i] = \int_0^{r_c} dr g_n(r) \frac{\partial^n \rho_i}{\partial r^n}(r, R_{ij}), \quad \frac{\partial^n \rho_i}{\partial r^n}(r) = \frac{\partial^n \rho_i}{\partial r^n}(r, R_{ij}) \quad (7)$$

where $g_n(r)$ is, again, a suitable radial weighting function. Generalizing this to all internal coordinates, a functional $F_n^{(m)}[i]$ can be defined over the n -th derivative of any m -body distribution function centered at atom i :

$$F_n^{(m)}[i] = \int_0^{\tau_c} d\tau g_n(\tau) \frac{\partial^n \rho_i}{\partial \tau^n}(\tau, \tau_{i_1 i_2 \dots i_m}),$$

$$\frac{\partial^n \rho_i}{\partial \tau^n}(\tau, \tau_{i_1 i_2 \dots i_m}) = \sum_{i_1 < i_2 \dots < i_m}^M H_n(\tau - \tau_{i_1 i_2 \dots i_m})$$

$$\times \mathcal{N}(\tau_{i_1 i_2 \dots i_m}, \sigma_\tau^2) \prod_{j=i_1}^{i_m} Z_j \quad (8)$$

where τ denotes the m -body internal coordinate, ρ_i is the m -body distribution function w.r.t atom i , g_n is the weighting function for the n -th derivative of ρ_i , H_n denotes the Hermite polynomial of degree n

and $\mathcal{N}(\tau_{i_1 i_2 \dots i_m}, \sigma_\tau^2)$ denotes the normalized Gaussian distribution. The Hermite polynomials arise due to the use of Gaussian PDFs and allow convenient computation of n derivatives of the distribution function at any point τ .

We note here that an alternative way to describe a (bounded) distribution in a compact form is through a moment expansion of the form:

$$G^{(m)}[i] = \int_0^{\tau_c} d\tau (\tau - \tau_{i_1 i_2 \dots i_m})^m g_m(\tau) \rho_i(\tau, \tau_{i_1 i_2 \dots i_m}) \quad (9)$$

where $G^{(m)}[i]$ denotes the m -th moment of the distribution centered at atom i . The set of m moments $G^{(m)}[i]$ would then form the local representation of the atom i . These moments can also be evaluated by placing a set of Gaussians (or any basis functions) on each atom i , and then evaluating the moments of the atomic density $\rho_i(\mathbf{r})$ w.r.t each atomic position within a radial cutoff \mathbf{r}_c :

$$G^{(m)}[i] = \int_0^{\mathbf{r}_c} d\mathbf{r} |\mathbf{r}|^m g_m(|\mathbf{r}|) \rho_i(\mathbf{r}),$$

$$\rho_i(\mathbf{r}) = \frac{1}{\sqrt{2\pi\sigma^2}} \sum_j \exp\left(-\frac{|\mathbf{r} - \mathbf{R}_{ij}|_2^2}{2\sigma^2}\right) \quad (10)$$

where $|\cdot|$ is any metric. This form has the advantage of being independent of many-body orders and the computational cost of evaluating these moments scales solely with the number of atoms within the cutoff radius \mathbf{r}_c . The integral can be simplified in spherical polar coordinates by expanding the density $\rho_i(\mathbf{r})$ in a basis set composed of spherical harmonics $Y_l^{m'}$ and orthogonal radial functions u_n (which is a common practice³⁶):

$$G^{(m)}[i] = \int_0^{\mathbf{r}_c} \int_0^{2\pi} \int_0^\pi dr d\theta d\phi r^{m+2} g_m(r) \sin(\phi)$$

$$\times \sum_{nlm'} c_{nlm'}^i u_n(r) Y_l^{m'}(\theta, \phi),$$

$$c_{nlm'}^i = \langle \rho_i(\mathbf{r}) | u_n(r) Y_l^{m'}(\theta, \phi) \rangle \quad (11)$$

Throughout our work we use the derivative formalism from eq. (8) since our numerical results indicated superior performance than the moments expansion in the internal coordinates (eq. (9)). However, the moment expansion in eq. (10), being independent of many-body terms, offers a promising alternative and could be the subject of a future work.

We have tested multiple weighting functions to identify the best combination. In particular, since these functionals correspond to correlation function averages of m -body interactions, we have tested the Harmonic, Morse⁴⁴, Lennard-Jones⁴⁵ potentials and simple decaying functions (power laws, exponential, gaussian decays

and their combinations) for 2-body terms. For 3-body terms we have tested Cosine Harmonic, Axilrod-Teller⁴⁶, Stillinger-Weber⁴⁷ potentials and a scaled Fourier series. Through trial and error combined with cross-validated hyper-parameter optimization, we have identified the following 5 suitable functionals corresponding to 2 and 3-body distributions:

$$F_0^{(2)}[i] = \int_0^{r_c} dr \left[e^{-\eta r} - \frac{\sqrt{2\pi}}{10(r+1)^3} \right] \rho_i(r, R_{ij}) \quad (12)$$

$$F_1^{(2)}[i] = \frac{\sqrt{2\pi}}{10} \int_0^{r_c} dr \frac{\partial_r \rho_i(r, R_{ij})}{(r+1)^6} \quad (13)$$

$$F_2^{(2)}[i] = \int_0^{r_c} dr e^{-\alpha r} \partial_r^2 \rho_i(r, R_{ij}) \quad (14)$$

$$F_0^{(3)}[i] = \int_0^\pi d\theta \frac{\sum_{n=0}^3 a_n \cos(n\theta)}{(R_{ij}R_{jk}R_{ik})^4} \rho_i(\theta, \theta_{jik}) \quad (15)$$

$$F_1^{(3)}[i] = \int_0^\pi d\theta \left[\frac{1 + \cos(\theta) \cos(\theta_{kji}) \cos(\theta_{ikj})}{(R_{ij}R_{jk}R_{ik})^4} \right] \times \partial_\theta \rho_i(\theta, \theta_{jik}) \quad (16)$$

where η , α , a_n and the various power laws are all hyper-parameters of the representation. Note the scaling functions of MBDF contributions $F_0^{(2)}$, $F_1^{(2)}$, $F_0^{(3)}$, $F_1^{(3)}$ being respectively reminiscent of Buckingham type-potential, softened London dispersion potential, Fourier series scaled by Lennard-Jones repulsion and Axilrod-Teller-Muto potential scaled by Lennard-Jones repulsion. The specific reason as to why this particular selection of weighting functions has proven advantageous will be subject of future research.

Figure 1 shows the effect of each functional on the learning capacity of MBDF for the task of predicting atomization energies of the QM9⁴⁸ dataset. It is apparent that both the derivative and many-body terms improve the learning capacity, albeit by different magnitudes.

Throughout our testing on the QM7⁴⁹, QM9⁴⁸ and QMugs⁵⁰ datasets, we have found these 2, 3-body functionals to be sufficient at discriminating between all of the molecular structures. Cases where the 2-body information does not suffice include homometric pairs, as already discussed many years ago¹⁴. And even 3- and 4-body information does not suffice for some cases, as recently discussed in Ref. 51. We note here that, whenever necessary, arbitrarily higher order derivative and many-body information could also be included in MBDFs at minimal increase in size, i.e. one additional term per order (See eq. (8)). In particular, we believe that the inclusion of the 4-body term as a functional of the dihedrals could further improve the learning capacity for conformational isomers. Inclusion of 4-body information has been shown to result in further improvements of learning curves⁵². Also note that the size of MBDF is invariant to the cutoffs used which can be raised to arbitrarily higher values while employing a suitable long-range functional (hence increasing the farsightedness of the representa-

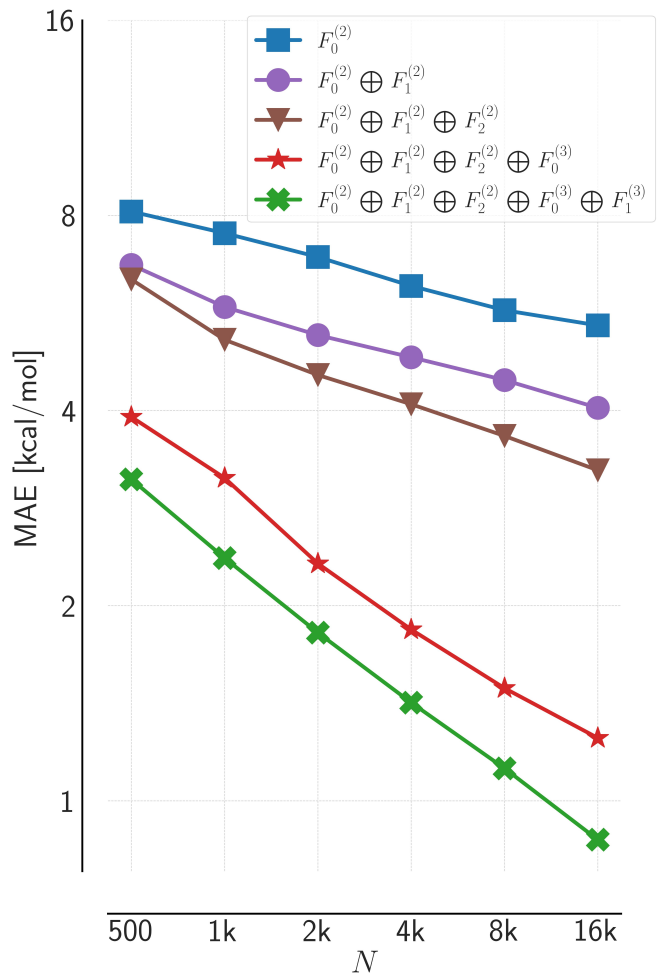


FIG. 1. MBDF based QML learning curves using concatenated increasingly higher order and body functionals (Eqs. (12-16)). Mean absolute error (MAE) of predicting atomization energies of the QM9⁴⁸ dataset is shown as a function of training set size N .

tion) without affecting the kernel evaluation cost. We further note that other weighting functions and response terms could also be useful for QML models of physical observables such as dipole moments, vibrational frequencies, heat capacities etc.

B. Density of functionals

MBDF is a local representation and its size scales linearly with the number of atoms in the system. In order to eliminate this scaling we can transform to the frequency space of MBDF functional values. The frequencies can be evaluated by normalizing the functional values to lie within an arbitrary range and then using, for e.g., kernel density estimation⁵³. For a finite set of MBDF functional values $\{X_i\}_{i=1}^{5M}$ over the range $[a, b]$, a "smooth histogram" of their frequencies can be constructed by

placing a set of kernel functions K at each point X_i :

$$f(u) = \frac{1}{5M} \sum_{i=1}^{5M} K(u, X_i) \quad (17)$$

where $f(u)$ gives the density of the samples at any point $u \in [a, b]$. If the set $\{X_i\}_{i=1}^{5M}$ are the MBDF functional values for any molecule, their distribution density can be evaluated using eq. (17). The density $f(u)$ can then be used as a global molecular representation whose size is independent of the number of MBDF functional values, and number of atoms by extension. The (dis-)similarity between two molecules A and B can be evaluated as, e.g., the l2-distance:

$$d(A, B)^2 = \int_{-c}^c du |f_A(u) - f_B(u)|^2 \quad (18)$$

where $[-c, c]$ is the normalization range chosen as $[-10, 10]$ in our work. The form of the density function used in our work is:

$$f_A(u) = \frac{1}{5M} \sum_{i=1}^{5M} \frac{\sqrt{|X_i|}}{\sqrt{2\pi\sigma_b}} \exp\left(-\frac{(u - X_i)^2}{2\sigma_b^2}\right) \quad (19)$$

where X_i are MBDF functionals for molecule A , σ_b is the variance of the Gaussian function and is a hyperparameter (also called bandwidth). Comparing with eq. (17), the function K is defined as:

$$K(u, X_i) := \frac{\sqrt{|X_i|}}{\sqrt{2\pi\sigma_b}} \exp\left(-\frac{(u - X_i)^2}{2\sigma_b^2}\right) \quad (20)$$

Note that this is a divergence⁵⁴ but not a kernel function because it is asymmetric:

$$\begin{aligned} K(x, y) &= \frac{\sqrt{|y|}}{\sqrt{2\pi\sigma_b}} \exp\left(-\frac{(x - y)^2}{2\sigma_b^2}\right) \\ &\neq \frac{\sqrt{|x|}}{\sqrt{2\pi\sigma_b}} \exp\left(-\frac{(x - y)^2}{2\sigma_b^2}\right) = K(y, x) \end{aligned} \quad (21)$$

This function is used because it weights the MBDF functional frequencies by the functional value itself resulting in the distance measurement (eq. (18)) being weighted by the difference in functional values. Another advantage of this function is that it eliminates the frequency of null values (or "ghost atoms") within the MBDF representation which might be present due to the procedure of zero-padding¹.

In our work we generate a separate density function $f(u)$ for each of the 5 MBDF functionals in eq. (11-15), and for each unique chemical element present in the dataset. These are then concatenated to form the global representation of the molecule. Alternatively, it could be done by using multivariate Gaussian functions for the density estimation. Let \mathbf{x}_i denote the 5-dimensional vector of MBDF functional values (eq. 11-15) for any atom i

in molecule A . Then the multivariate density function $f_A(\mathbf{u})$ of this molecule can be evaluated as :

$$f_A(\mathbf{u}) = \frac{1}{M} \sum_{i=1}^M K(\mathbf{u}, \mathbf{x}_i) \quad (22)$$

$$f_A(\mathbf{u}) = \frac{1}{M} \sum_{i=1}^M \frac{(\mathbf{x}_i^T \mathbf{x}_i)^{1/4}}{\sqrt{2\pi\sigma_b}} \exp\left(-\frac{(\mathbf{u} - \mathbf{x}_i)^T (\mathbf{u} - \mathbf{x}_i)}{2\sigma_b^2}\right) \quad (23)$$

The l2-distance between molecules A and B then takes the form:

$$d(A, B)^2 = \int d\mathbf{u} (f_A(\mathbf{u}) - f_B(\mathbf{u}))^T (f_A(\mathbf{u}) - f_B(\mathbf{u})) \quad (24)$$

where the integral is over the normalization region. Since the former method generates a more compact representation we have chosen to work with it. The abbreviation DF (Density of functionals) will be used throughout for this global representation.

C. Numerical analysis

The DF method allows generating a representation that does not scale with the number of atoms in the system. However, in order to use it as a feature vector the density functions have to be discretized. Through convergence testing we have set the grid spacing to 0.2 throughout our work. However, we note that this grid spacing could be changed for a different data-set in order to achieve the desirable accuracy vs computational cost trade-off. Furthermore, DF corresponds to a flattened feature vector which can be used with global kernels (or other ML methods), and which exhibits superior performance when compared to a straightforward concatenation of all MBDF rows (see Figure 2). The flattened MBDF representation is generated by sorting the MBDF matrix of each molecule by the row norm, and then flattening the matrix by concatenation of the rows to vectorize it¹.

Figure 3 shows molecular fingerprints generated using the 1 and 5 functional DF representations for three diverse and relevant organic molecules (glucose, uric acid, and testosterone) on the same grid. For each molecule, a distinct fingerprint is obtained, with peak-positions depending on the local chemical environment of each atom. Consequently, peaks of atoms with chemically similar environments are located closer to each other. Peak heights encode both number and type (because of the density estimate being weighted) of chemical environments [See Eq. 20]. Figure 3 demonstrates that for molecules with increasing size, corresponding DF based fingerprints will

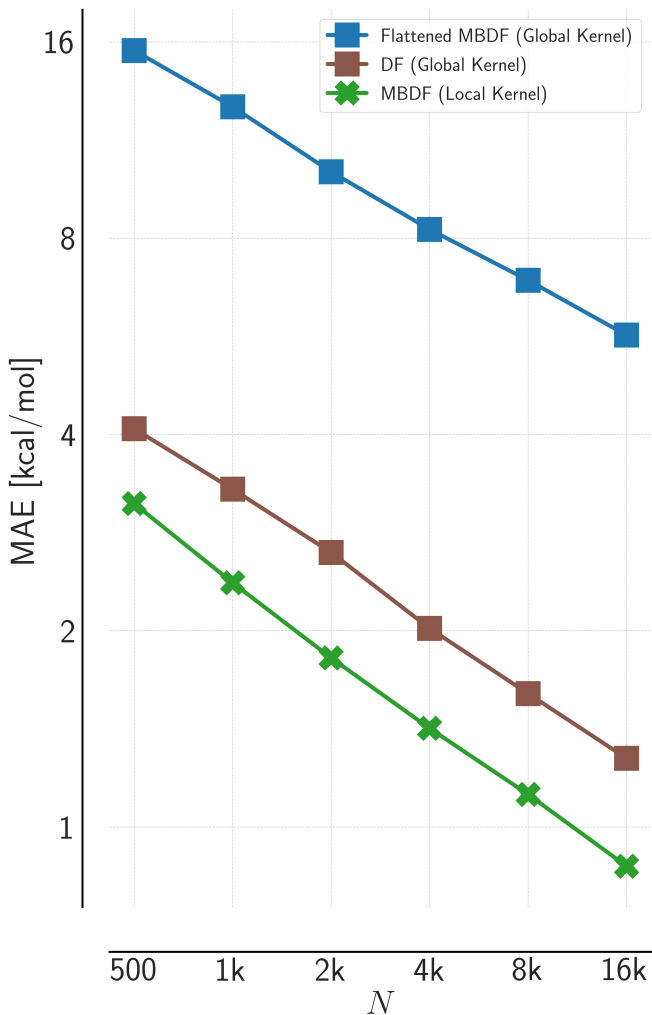


FIG. 2. QML learning curves for MBDF with local kernel, DF (global), and flattened MBDF (global and sorted by row norm). Mean absolute error (MAE) of predicting atomization energies of the QM9⁴⁸ data-set as a function of training set size N .

grow in magnitude, not in size. In the SI, we also show how DF fingerprints distinguish conformational isomers, as exemplified for the chair and boat conformations of cyclohexane.

III. METHODS AND DATA

A. Kernel ridge regression

The ML method that we focus on, and use throughout this work, is the supervised learning method called Kernel ridge regression^{18,39} (KRR). This method has been covered extensively earlier^{1-3,34,35} so we skip the details here.

The kernel functions^{55,56} we use in our work along with

global representations are the Gaussian kernel,

$$k(\mathbf{x}_I, \mathbf{x}_J) = \exp\left(-\frac{\|\mathbf{x}_I - \mathbf{x}_J\|_2^2}{2\sigma^2}\right) \quad (25)$$

and Laplacian kernel,

$$k(\mathbf{x}_I, \mathbf{x}_J) = \exp\left(-\frac{\|\mathbf{x}_I - \mathbf{x}_J\|_1}{\sigma}\right) \quad (26)$$

where \mathbf{x}_I denotes the representation vector of molecule I .

The kernel function used for the local representations FCHL19, SOAP and MBDF is a summation of atomic kernels:

$$k(\mathbf{M}_I, \mathbf{M}_J) = \sum_{a \in i} \sum_{b \in j} k^l(\mathbf{x}_{Ia}, \mathbf{x}_{Jb}) \quad (27)$$

with the local Gaussian kernel:

$$k^l(\mathbf{x}_{Ia}, \mathbf{x}_{Jb}) = \delta_{Z_a, Z_b} \exp\left(-\frac{\|\mathbf{x}_{Ia} - \mathbf{x}_{Jb}\|_2^2}{2\sigma^2}\right) \quad (28)$$

the local Laplacian kernel:

$$k^l(\mathbf{x}_{Ia}, \mathbf{x}_{Jb}) = \delta_{Z_a, Z_b} \exp\left(-\frac{\|\mathbf{x}_{Ia} - \mathbf{x}_{Jb}\|_1}{\sigma}\right) \quad (29)$$

or the local exponential kernel with the Euclidean norm:

$$k^l(\mathbf{x}_{Ia}, \mathbf{x}_{Jb}) = \delta_{Z_a, Z_b} \exp\left(-\frac{\|\mathbf{x}_{Ia} - \mathbf{x}_{Jb}\|_2}{\sigma}\right) \quad (30)$$

where \mathbf{M}_I denotes the representation matrix of molecule I , \mathbf{x}_{Ia} denotes the representation vector of atom a within molecule I and δ_{Z_a, Z_b} denotes a Kronecker Delta over the nuclear charges Z_a, Z_b which restricts the similarity measurement between atoms of the same chemical element³⁴. Other kernel functions will also be tested in the future^{40,57,58}.

Throughout this study, we evaluate performance of ML methods through learning curves for the task of predicting physical properties of molecular systems. Learning curves quantify the model prediction error ϵ (often measured as mean absolute error (MAE)) against the number of training samples N and are key to understand the efficiency of ML models. It is generally known^{18,59,60} that they are linear on a log-log scale,

$$\log(\epsilon) \approx I + S \log(N) \quad (31)$$

where I is the initial error and S is the slope indicating model improvement given more training data. We also note that according to the central limit theorem the distribution of the errors ϵ approaches the normal distribution with standard deviation $\frac{\sigma}{\sqrt{N}}$, and mean 0 as

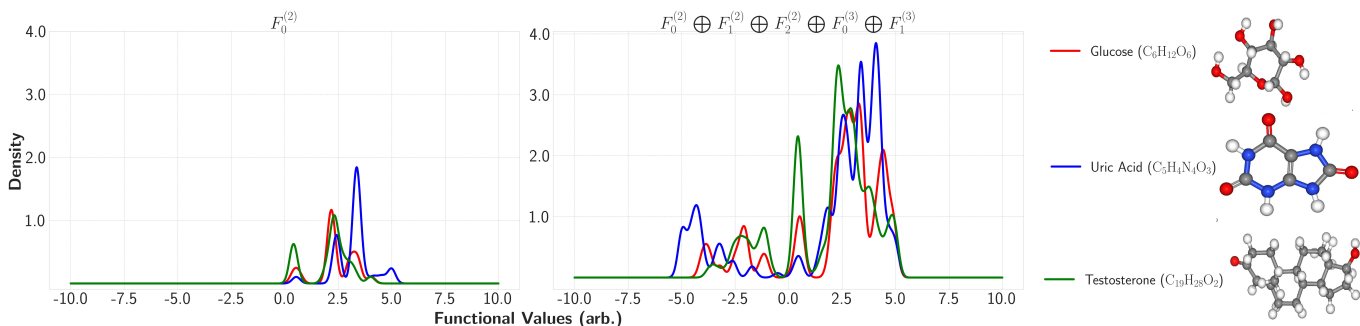


FIG. 3. Two-body (left) and three-body (right) DF versions (Eqs. 12, 15) representations for Glucose, Uric Acid, and Testosterone.

$N \rightarrow \infty$. Hence eq. (31) becomes :

$$\log(\varepsilon) \approx \log(\sigma) - \frac{1}{2} \log(N) \quad (32)$$

B. Hyperparameter Optimization

The current form of the representations has been optimized for Kernel based learning models. It depends on the weighting functions used and a number of hyperparameters which include variances (σ_r, σ_θ) of the Gaussian PDFs, weighting function hyperparameters mentioned in eq. (12)-(16), and bandwidth σ_b for the DF representation. The hyperparameter optimization was done on a random subset of two thousand molecules from the QM7 dataset⁴⁹, and then kept fixed for all other data-sets. We note that further improvements might be possible if they had been optimized simultaneously on all data-sets. The weighting functions $g_n(\tau)$ in eq. (8) were chosen by straightforward screening of the functions mentioned earlier. The optimization minimized the atomization energy prediction errors on the QM7 subset using Gaussian Process (GP) based Bayesian Optimization (BOpt)³⁹. Starting with a Gaussian prior, the method fits a posterior distribution over the objective function using successive function evaluations. The posterior distribution is then used to construct an efficient acquisition function which can be optimized using, for instance, a quasi-Newton method to determine the next query point. Table 1 shows the optimized hyperparameter values used throughout this work.

We used the scikit-optimize⁶¹ implementation of GP based BOpt using the default Matérn kernel with unit variance and the limited memory BFGS optimizer⁶² for the acquisition function. In order to enable comparison to other representations (such as FCHL or SOAP) that rely on distance cutoffs, we have chosen to set interatomic distance cutoff r_c for MBDF to 6 Å throughout this work. We note that larger cutoffs for MBDF would not change its size.

All MBDF functionals were evaluated using the trapezoidal numerical integration method. The grid spacing

Parameter	Value
σ_r	1
σ_θ	2
η	10.8
α	1.5
a_0, a_1, a_2, a_3	3, 100, -200, -164
σ_b	0.07
r_c (Å)	6

TABLE I. MBDF and DF hyperparameters after optimization on atomization energies of QM7⁴⁹ subset.

for discretizing DF densities has been set to 0.2 throughout our work as noted earlier. The bandwidth $\sigma_b = 0.07$ was found to work well on the QM7 subset however it is recommended to be screened once (in the range $\sim [0.01, 1]$) along with the grid-spacing when using with other datasets. The Numpy⁶³ and Numba⁶⁴ libraries are used in the representation generation code.

C. Data and Code

The QM9 dataset⁴⁸ consists of $\sim 134k$ small organic molecules with up to 9 heavy atoms (C, N, O, F). The calculations were performed at the B3LYP/6-31G(2df,p)⁶⁵⁻⁶⁷ level of theory.

QMugs is a dataset containing $\sim 665k$ biologically and pharmacologically relevant drug-like molecules. It consists of larger molecules than QM9 with up to 100 heavy atoms (C, N, O, F, P, S, Cl, Br, or I) per molecule. The training and predictions were performed on the DFT (ω B97X-D/def2-SVP)^{68,69} values reported in the dataset. The QMugs subsets we used for Figure 5 were drawn at random and consist of 20k molecules. Throughout, we used zero-padding for all representations studied in order to accommodate training and test molecules smaller than the maximum present in the data.

In order to keep the FCHL19 and SOAP kernel evaluations computationally tractable, we have (a) restricted ourselves to a maximum 100 atoms per QMugs-molecule, and (b) reduced the default hyperparameters of the

FCHL19 and SOAP representations to $nRs2 = 12$, $nRs3 = 10$, $r_{cut} = 6\text{\AA}$ and $n_{max} = l_{max} = 3$, $\sigma = 0.1$, $r_{cut} = 6\text{\AA}$, respectively. For consistency, we used the same parameters for all other results reported in this article. These two versions of the representations with the reduced basis sets are denoted as FCHL19* and SOAP* in all reported figures. Note that the latter choice of hyperparameters negligibly deteriorates the predictive accuracy for QM9 (as assessed below and when comparing to the published prediction errors on QM9 for FCHL19 and SOAP2013). For FCHL19 and SOAP based prediction errors reported here within for QMugs, it could still be that the accuracy could improve further if these parameters were optimized.

Figure 4 also includes results for QML models based on the 2- ($k = 2$) and 3-body ($k = 3$) Many-Body Tensor Representations (MBTR)²² and a variant⁷⁰ of the Atom Centered Symmetry Functions²⁰ (ACSF) as implemented in the QMLcode library⁷¹. The MBTR representations were generated with the same hyperparameters as those used in Ref. 33 for the 10k training point on the QM9 dataset.

Throughout our work, the FCHL19, SLATM and ACSF representations were generated using the QMLcode library⁷¹, SOAP was generated using the Dscribe library⁷² with the default gaussian type radial basis functions, MBTR was generated using the qmmlpack library⁷³ and SchNet⁷⁴, PaiNN⁷⁵ were built and trained using the SchNetPack⁷⁶ library. Allegro⁷⁷ was built and trained using the nequip⁷⁸ code⁷⁹ based on the E(3)-NN framework^{80,81}.

For FCHL19, SOAP and ACSF we employed the local Gaussian (eq. (28)), for SLATM, MBTR and DF we use the global Gaussian (eq. (25)) and for CM, BOB we use the global Laplacian (eq. (26)) kernels respectively. For MBDF we used the local Gaussian kernel on the MD17 dataset and the local exponential (eq. (30)) kernel for all other models. These choices were made based on the best performances for each representation. All kernel evaluations were performed using the QMLcode library.

IV. RESULTS

A. Atomization Energies

QM9

Figure 4 a) shows learning curves for QM9 and the size (dimension of feature vector) of the representation arrays in the legend. For the task of predicting atomization energies, local representations have previously been shown to be more efficient^{34,35}. Results for the local representations FCHL19 and SOAP are closely reproduced, and reach chemical accuracy after training on less than 10k molecules³⁴. Among the global representations, SLATM has previously also been shown^{34,37} to perform quite well reaching chemical accuracy after training on $\sim 9k$ molecules although it shows a smaller slope

at larger training sizes. This is closely followed by MBDF which reaches chemical accuracy after training on $\sim 10k$ molecules (less than 10% of the dataset). The global DF representation also performs decently well reaching chemical accuracy at $\sim 32k$ training data. The local ACSF representation shows a larger offset but a better slope and it reaches chemical accuracy at $\sim 50k$ training set size. We note here that for consistency with the other representations used in this work, we did not optimize the hyperparameters of the MBTR representation on every training point, but rather kept them fixed throughout. Only the KRR hyperparameters were optimized at each training set size as with all other representations used here. The 3-body MBTR reaches chemical accuracy at $\sim 60k$ training set size while the 2-body MBTR performs better than the other 2-body representations, BOB and CM. We have also included the recently introduced constant size Persistence Images⁸²(PI) representation for comparison.

Note that MBDF has the smallest size, requiring only 5 numbers per atom (145 dimensions for QM9 molecules). By contrast, other local representations such as FCHL19, SOAP require ~ 400 numbers per atom, while ACSF uses a 150 dimensional feature vector per atom. Encouragingly, and despite its compact size, MBDF outperforms most of the other larger representations with the exception of SOAP and FCHL. We note here that while the size of the global DF representation is larger than MBDF, it utilises a global kernel implying training and prediction cost invariance with respect to system size.

This compactness of the representation translates into faster ML model evaluation timings. This is shown in Figure 4 b) which plots the trade-off between training and prediction timings vs. training data needs for reaching mean absolute prediction errors of atomization energies of 1 kcal/mol. We note that there are only two representations located on the Pareto-front, FCHL18³⁵ and MBDF [this work]. We also point out that currently the best performing model on the QM9 dataset is the recently proposed Wigner Kernels method⁸³ which is not included in this study.

As noted earlier, local kernels based on representations such as FCHL18/19, SOAP, or ACSF exhibit very good training data efficiency, but this comes at the expense of a larger computational overhead. The exception is the local MBDF based kernel which achieves the fastest training timing of ~ 0.07 compute node minutes (14k training molecules) due to its compact size. Predictions on 100k QM9 molecules using the local MBDF kernel are made in ~ 1.46 compute node minutes which translates to an unprecedented chemically accurate navigation rate of ~ 1140 molecules/second. SLATM being close to the Pareto front, and the DF representation, both represent fast global kernel based KRR models. While requiring more training data than SLATM in order to reach chemical accuracy, DF has the advantage that it is largely invariant with respect to system size (see below). For the sake of completeness, Fig. 4 b) also includes results for the deep learning based models SchNet⁷⁴, PaiNN⁷⁵

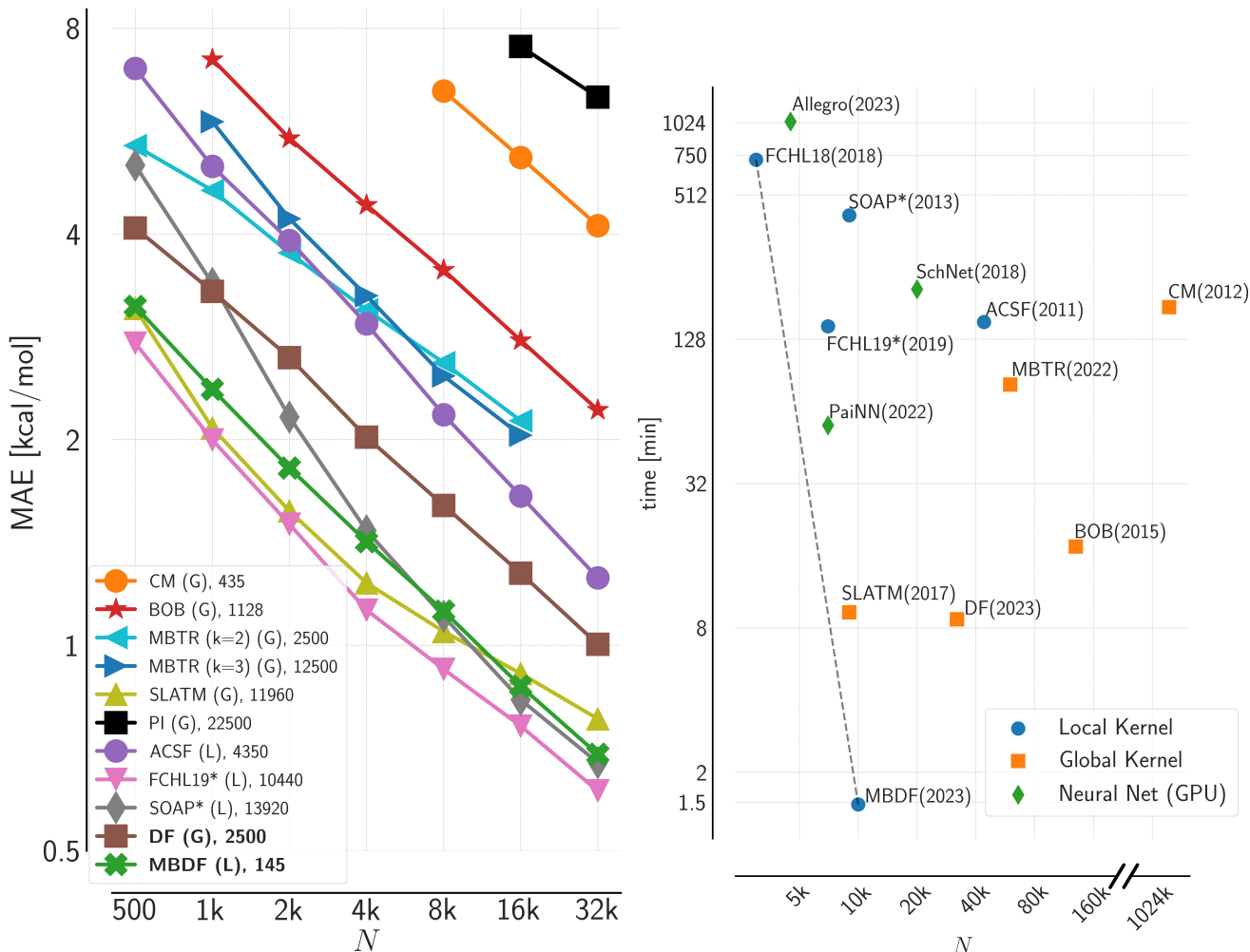


FIG. 4. MBDF/DF performance and comparison on atomization energies from QM9 data set (drawn at random from $\sim 134k$ organic molecules)⁴⁸. a) (Left) Mean absolute error (MAE) of prediction as a function of training set size for representations CM¹, BOB³⁸, MBTR²², SLATM³⁷, PI⁸², ACSF^{20,70}, FCHL19³⁴, SOAP³⁶. Numbers in legend denote representation size (feature vector dimensions), G and L denote Global and Local kernels, respectively. b) (Right) Timing for training and testing as a function of training set size required for making chemically accurate (MAE = 1 kcal/mol) predictions on 100k molecules. Blue, red, and green points indicate local kernels, global kernels, and neural network, respectively. Dashed gray line corresponds to the optimal Pareto front. For SchNet⁷⁴, PaiNN⁷⁵, Allegro⁷⁷ an Nvidia RTX 3070 GPU has been used. All other timings were evaluated on a compute node equipped with a 24-core AMD EPYC 7402P @ 3.3 GHz CPU and 512 GB RAM. Timings for FCHL18³⁵, BOB, CM are estimated using smaller kernels (not taking into account kernel inversion). Asterisk denotes representations with reduced hyperparameters used in this work. N values for ACSF, MBTR, BOB, CM estimated via extrapolation. Numbers in brackets denote year of publication.

and the current state-of-the-art, Allegro⁷⁷ which were all trained on a GPU. The reported timing for SchNet refers to 3000 epochs of training on 20k molecules and predictions of 100k molecules taking about 3 h: 27 min and 7 sec respectively. For PaiNN the reported timing corresponds to 1000 epochs of training on 7k molecules which took 0 h: 56 mins and a prediction time of 9 sec. Allegro reached chemical accuracy after training on 4500 molecules for 728 epochs, with early stopping, which took 17 h: 8 min while the prediction on 100k molecules took ~ 7 mins (using a maximum possible batch size of 5 on the used GPU).

MBDF achieves the fastest training time out of all models and the fastest prediction rate among the kernel based models. Numerical results for porting KRR results based on FCHL19 to GPUs⁸⁴ would suggest that it seems likely for the prediction rate to increase significantly once MBDF is reimplemented in CUDA.

QMugs

We have tested the generalizability of our method to larger systems and more diverse chemistries using the

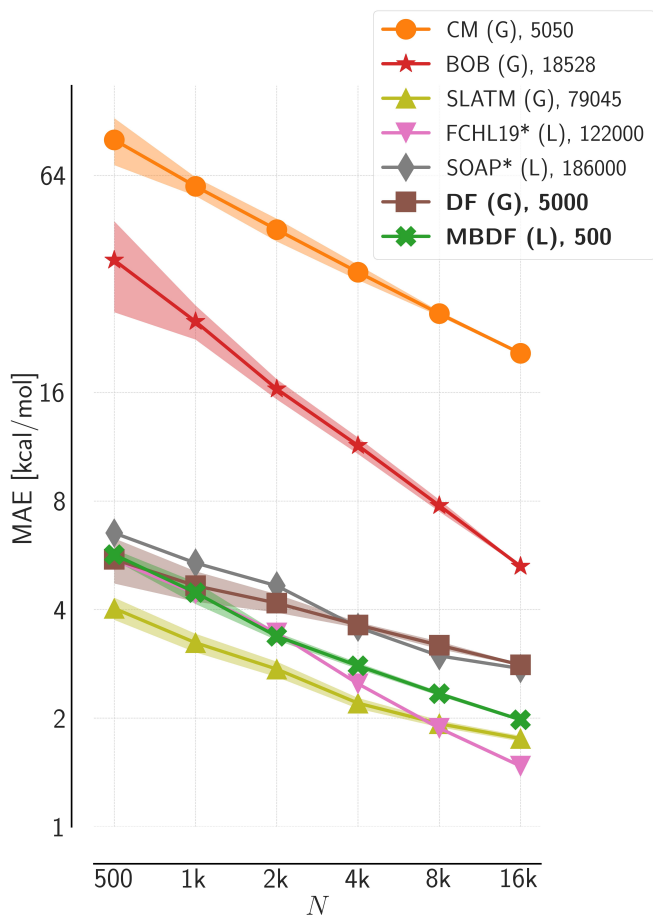


FIG. 5. MBDF/DF performance and comparison to CM¹, BOB³⁸, SLATM³⁷, FCHL19³⁴, and SOAP³⁶ representation based atomization energy estimates using the QMugs ($\sim 667k$ organic molecules with up to one hundred heavy atoms) data set⁵⁰. Training and testing data drawn at random. Prediction mean absolute errors (MAE) on holdout test set of 4k molecules shown as a function of training set size. Numbers in legend denote representation size (feature vector dimensions), G and L denote Global and Local kernels respectively. Shaded region denotes the standard deviation across 4 different learning curves (except for FCHL19 and SOAP for which only one learning curve was tractable). Asterisk denotes representations with reduced hyperparameters used in this work.

QMugs⁵⁰ data set. Figure 5 shows the atomization energy learning curves. Due to the large variety in the dataset, the predictive error is larger for all representations than their QM9 counterparts even when predicting on a much smaller test set. MBDF reaches ~ 2 kcal/mol prediction error after training on 16k molecules. This is better than the QML based neural network predictions published in Ref. 85, and similar to the Δ -QML numbers they also report. In terms of speed, generating the local MBDF kernel for training and testing on 20k molecules on this dataset takes ~ 1.8 compute node mins (see below) which corresponds to a navigation rate of ~ 185 molecules/second. By comparison, this is sub-

stantially faster than the GPU based prediction rates of approximately 50 and 5 molecules per second for the direct and Δ -learning (using GFN2-xTB⁸⁶) based ML models, respectively using the convolutional neural network reported in Ref. 85. Only SLATM and FCHL19 exhibit lower off-set than MBDF, while the performance for SOAP and DF is similar, albeit slightly worse than MBDF. As mentioned before, however, in order to make FCHL19 and SOAP tractable, we have dramatically reduced the hyper parameters. In particular, we believe that the learning efficiency of SOAP for QMugs is being reduced due to the use of small basis sets ($n_{max} = l_{max} = 3$). Note that no representation reaches chemical accuracy within 16k training molecules, indicating that QMugs possesses substantially more chemical diversity than QM9.

In terms of representation sizes, MBDF again remains the smallest representation since it still requires only 5 dimensions per atom regardless of the chemical composition. However, being a local representation, on average its size increases ~ 3.4 times compared to QM9. FCHL19 and SOAP, on the other hand, now require more than 1000 dimensions to represent each atom for this larger dataset. CM, BOB, FCHL19, and SOAP show larger than 10 fold increase in the representation size compared to QM9, followed by SLATM which shows an increase of ~ 6.6 times. This results in a considerable increase in the train/test time (*vide infra*) which precludes the straightforward application of these representations to the entire QMugs dataset. The DF representation changes the least in size since it does not formally scale with number of atoms but only with number of different chemical elements. Consequently, its size doubles compared to QM9 since a separate density function is generated for each unique chemical element in the dataset using eq. (19) as mentioned earlier.

QM7b and MD17

Figure 2 in the SI shows learning curves for the QM7b^{87,88} atomization energies and the size (dimension of feature vector) of the representation arrays in the legend. Similar trends in performance and representation size noted so far are observed on this dataset as well. Figure 3 in the SI shows learning curves of energies for a few molecules from the revised^{89,90} MD17^{91,92} molecular dynamics dataset. Although the comparative performance trend on this dataset is similar to the others, we note that the chosen functionals for MBDF and the current representation hyperparameters are not optimized for potential energy surface learning. Furthermore, the implementation of gradients for MBDF to enable force based learning should significantly enhance the performance for such tasks as was shown⁸⁹ for the FCHL19 representation. However, the relatively larger difference in performance between MBDF and FCHL19 on this dataset might indicate that compact representations are

sufficient for regression through equilibrium structures across CCS while more verbose representations are required for potential energy surface learning.

B. Timings

Figure 6 shows scaling plots of kernel evaluation timings across both QM9 and QMugs datasets for various representations and as a function of training set size. As one would expect, the off-set increases systematically with increasing representation and training molecule size. More specifically, for the larger molecules of QMugs, the FCHL19 and SOAP kernel evaluations become rapidly intractable very quickly with the 16k kernel (Fig. 5) already taking an entire compute node day. Encouragingly and in stark contrast, DF, being a size invariant representation, shows hardly any change in computational overhead when moving from the small QM9 molecules to the much larger QMugs molecules.

For context, the time required in the kernel inversion step for each training kernel is shown as well. The bottleneck crossover from kernel generation ($\mathcal{O}(n^2)$) to the inversion step ($\mathcal{O}(n^3)$) occurs rather late. When using Cholesky decomposition it occurs for MBDF at $N \sim 64k$ training molecules. For less compact representations (for SLATM and larger) the same cross-over occurs at training set sizes that exceed ~ 1 M. As demonstrated above, chemical accuracy is already achieved at substantially smaller training set sizes. Consequently and contrary to popular belief, for any of the more modern and accurate representations, kernel inversion does not constitute a bottleneck.

Table 2 reports the kernel evaluation and representation generation timings for both the QM9 dataset (130k molecules) and the QMugs subset (20k molecules) used in our work. It can be seen that MBDF reduces the local kernel evaluation timings from days to a few minutes for both small and large molecules. For the representation generation step we note that our code is currently written in Python and uses the Numba⁶⁴ library and could be further optimized with a low-level implementation. However, the current timings as well do not affect the overall QML model cost much given the kernel evaluation bottleneck.

C. Performance for molecular quantum properties

We assessed the generalization capacities of MBDF/DF on physical properties other than atomization energies. Figure 7 shows the learning curves for the task of predicting 8 important molecular quantum properties from the QM9 dataset. These include the highest occupied molecular orbital (HOMO), lowest unoccupied molecular orbital (LUMO) eigenvalues and the HOMO-LUMO gap, internal energy at 0 K (U_0), dipole moment norm ($|\mu|$), static isotropic polarizability

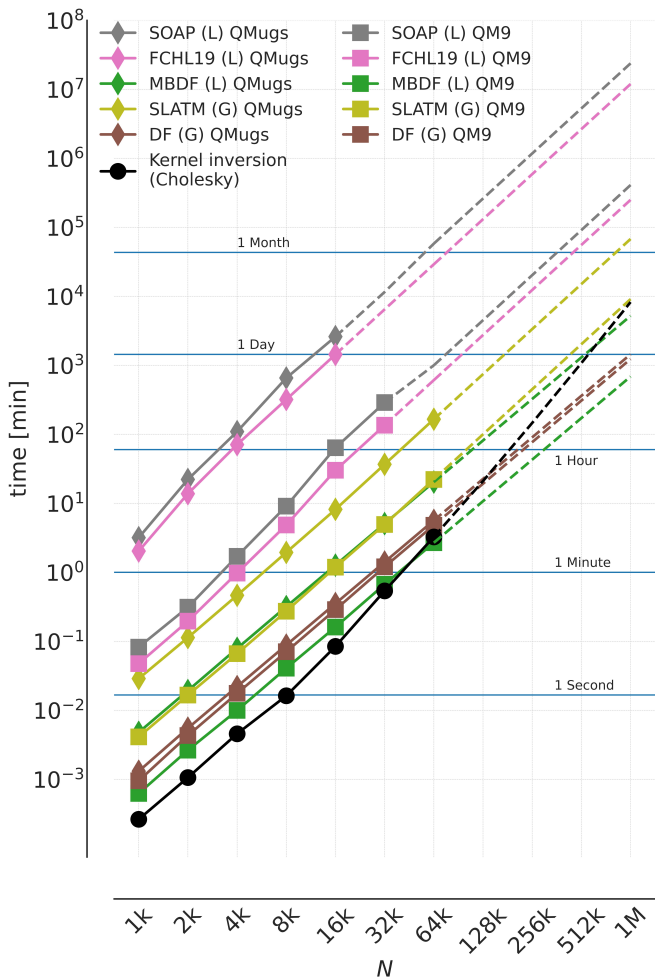


FIG. 6. Compute node time required for kernel inversion and evaluation as a function training set sizes N drawn from QM9 (squares) and QMugs (diamonds) datasets. QML results shown for SOAP³⁶, FCHL19³⁴, SLATM³⁷, and MBDF and DF. Dotted lines indicate extrapolation (using quadratic (kernel evaluation) and cubic (kernel inversion) polynomial fits). G and L denote Global and Local kernels, respectively. Compute node: 24-core AMD EPYC 7402P @ 3.3 GHz CPU with 512 GB RAM.

(α), zero point vibrational energy (ZPVE) and heat capacity (C_v). Due to substantial computational costs, the KRR hyper-parameters were not optimized at each training size for the FCHL19 and SOAP representations, and we picked the same parameters as those used for learning atomization energies in figure 4. We reproduce earlier trends among intensive and extensive properties when using local/global kernels^{3,93}. MBDF and DF match this trend: They perform better on extensive and on intensive properties, respectively.

Again, note that the performance on these properties of MBDF/DF could be further improved by including different functionals suited to the property, or by augmenting them with response terms as was done for the FCHL19 representation⁹³. It would also be interesting

Representation	QM9 130k Molecules			QMugs 20k Molecules		
	t_{rep} [min]	t_{kernel} [min]	Dimension	t_{rep} [min]	t_{kernel} [min]	Dimension
CM ^a (G)	0.186	2.862	435	0.012	1.146	5050
BoB ^a (G)	0.216	7.296	1128	1.362	3.396	18528
SLATM ^a (G)	18.60	86.32	11960	15.76	14.58	79045
FCHL19 ^a (L)	0.846	1071	10440	1.764	1566	122000
SOAP ^b (L)	0.216	1873	13920	0.246	2925	186000
MBDF (L)	1.626	11.81	145	4.182	1.848	500
DF (G)	2.262	12.16	2500	2.442	0.996	5000

TABLE II. Compute node times for generating representations (t_{rep}) and kernel matrices (t_{kernel}) for 130k molecules from the QM9 dataset and 20k molecules from the QMugs dataset. Global and Local kernels are again denoted by (G) and (L) respectively. Representations with superscript *a* were generated with QMLcode⁷¹ library and *b* with the Dscribe⁷² library. Compute node: 24-core AMD EPYC 7402P @ 3.3 GHz CPU and 512 GB RAM.

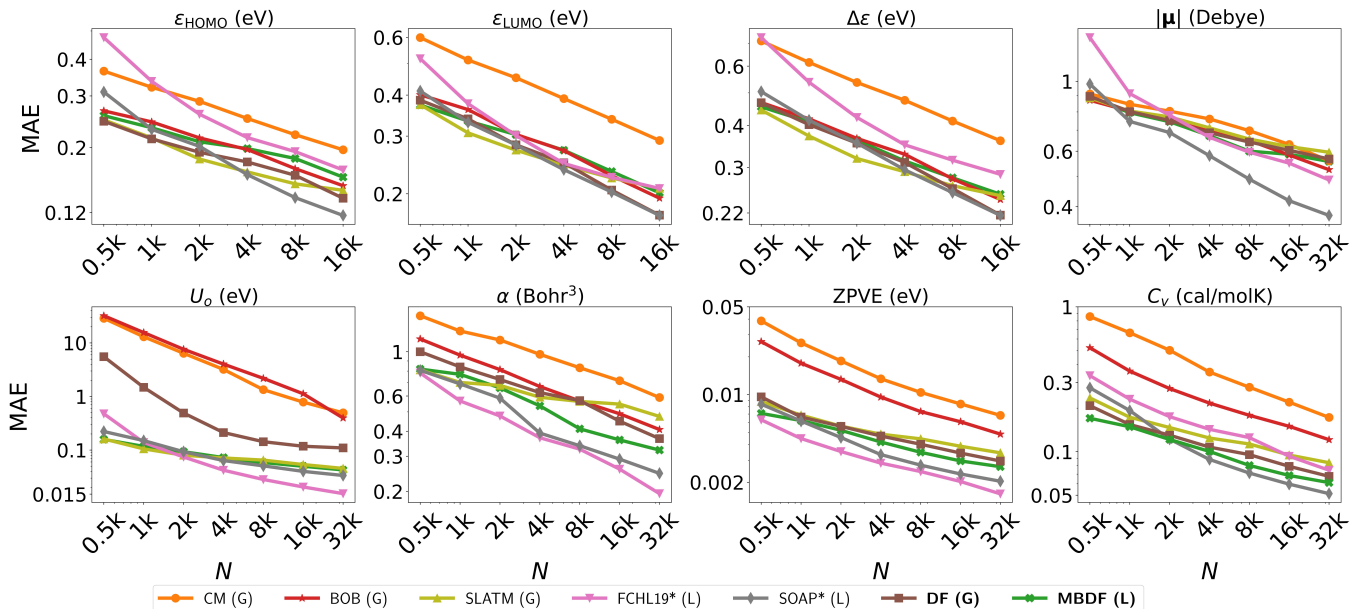


FIG. 7. Learning curves for various representations in QML models of highest occupied molecular orbital (HOMO), lowest unoccupied molecular orbital (LUMO) eigenvalues, HOMO-LUMO gap ($\Delta\epsilon$), internal energy at 0 K (U_0), dipole moment norm ($|\mu|$), static isotropic polarizability (α), zero point vibrational energy (ZPVE), and heat capacity (C_v) from the QM9 dataset. G and L denote Global and Local kernels, respectively. Asterisk denotes representations with reduced hyperparameters used in this work.

to see how the learning capacities across these different physical properties is affected by the inclusion of higher order functional terms.

V. CONCLUSION

We have introduced ultra-compact atomic local many body distribution functional (MBDF) and global density of functionals (DF) representations for use within kernel ridge regression based Quantum Machine Learning (QML) models for rapid sampling of chemical compound space. MBDF/DF can accurately describe any atom/molecule using a minimal number of discrete elements and thereby reduce QML training and prediction times by multiple orders of magnitude for small and

large molecules. MBDF and DF correspond to functionals of analytical weighted many body distributions in interatomic distances and angles, as well as their derivatives. Chemical identity is encoded as a prefactor to the atomic functionals. DF is a weighted density estimations of MBDF, i.e. a global molecular fingerprint that is invariant with respect to number of atoms (not number of chemical elements).

We have demonstrated predictive power competitive with the state-of-the-art for a variety of quantum physical properties, as encoded in the QM9 dataset⁴⁸. On the QM9 dataset MBDF reaches a MAE of atomization energies of only 0.69 kcal/mol after training on 32k molecules while using only 5 dimensions to describe an atom. Regarding different molecular properties, it is beneficial to use DF representation along with a global kernel for in-

tensive properties, and MBDF along with a local kernel for the extensive properties. MBDF and DF generalize also well to other compound spaces, as evinced for the chemically more diverse QMugs dataset⁵⁰ consisting of substantially larger molecules: After training on 16k molecules, MBDF reaches a peak MAE for atomization energies of 1.97 kcal/mol while still using only 5 dimensions per atom. Corresponding training and prediction times for both data-sets is ~ 2 compute node time minutes for MBDF based models. Furthermore, our results indicate that using MBDF/DF brings the train/test timings of kernel based ML models to their "lower-bound" as imposed by the kernel inversion bottleneck for both small and large molecules.

We have analyzed the comparative performance for the sampling cost vs. training set size needs to reach chemical accuracy for predicting atomization energies in the QM9 data-set. MBDF has extended the corresponding optimal Pareto front towards minimal time requirements.

While the numerical evidence collected is indicative of a surprising effectiveness of MBDF, it is clear that the truncations used in this work may lead to lack of uniqueness. However, neither within QM9 nor within the QMugs subset we sample, have we encountered a case where using this small set of functionals maps two different molecular structures to the same feature vector. Furthermore, the likelihood of uniqueness can easily be increased by inclusion of higher order derivatives and many-body terms. More rigorous numerical analysis would be desirable to quantify this trend.

Thanks to its numerical efficiency, we believe that this approach holds great promise for further accelerating the virtual discovery of novel molecules and materials. Furthermore, this framework provides a possible solution to the general problem of unfavourable scaling due to i) inclusion of higher order many body and long range physics and ii) applying these ML models to larger molecules

with greater chemical diversity. Future work will deal with extension of the representations as described to deal with various types of conformers, and an assessment of its sensitivity to changes in molecular structures.

VI. ACKNOWLEDGMENTS

D.K. is thankful for discussions with B. Huang, S. Krug, D. Lemm, M. Sahre, and J. Weinreich. O.A.v.L. has received funding from the European Research Council (ERC) under the European Union's Horizon 2020 research and innovation programme (grant agreement No. 772834). O.A.v.L. has received support as the Ed Clark Chair of Advanced Materials and as a Canada CIFAR AI Chair.

VII. SUPPLEMENTARY MATERIAL

See supplementary material for QM7b⁸⁷, MD17⁸⁹⁻⁹² learning curves and a figure showing the transition of cyclohexane from chair to boat conformation alongside the response by its DF fingerprint. It also contains heat maps showing ideal KRR hyperparameters to be used with the MBDF representation and kernel PCAs of some molecules from the QM7b dataset.

VIII. CODE AND DATA AVAILABILITY

Python script for generating the MBDF and DF representations is available at <https://github.com/dkhan42/MBDF>. Train/test split of the QM7 dataset used for optimizing representation hyperparameters, other data and code for reproducing the results in this study and some tools for performing KRR are openly available at <https://github.com/dkhan42/QML>.

-
- [1] M. Rupp, A. Tkatchenko, K.-R. Müller, and O. A. von Lilienfeld, *Phys. Rev. Lett.* **108**, 058301 (2012).
- [2] O. A. von Lilienfeld, *Angewandte Chemie International Edition* **57**, 4164 (2018), <http://dx.doi.org/10.1002/anie.201709686>.
- [3] F. A. Faber, L. Hutchison, B. Huang, J. Gilmer, S. S. Schoenholz, G. E. Dahl, O. Vinyals, S. Kearnes, P. F. Riley, and O. A. von Lilienfeld, *Journal of Chemical Theory and Computation* **13**, 5255 (2017), pMID: 28926232, <https://doi.org/10.1021/acs.jctc.7b00577>.
- [4] T. Ho and H. Rabitz, *J. Chem. Phys.* **104**, 2584 (1996).
- [5] S. Manzhos and T. Carrington, Jr., *J. Chem. Phys.* **125**, 084109 (2006).
- [6] J. Behler and M. Parrinello, *Phys. Rev. Lett.* **98**, 146401 (2007).
- [7] A. P. Bartók, M. C. Payne, R. Kondor, and G. Csányi, *Phys. Rev. Lett.* **104**, 136403 (2010).
- [8] C. M. Handley and P. L. A. Popelier, *The Journal of Physical Chemistry A* **114**, 3371 (2010), pMID: 20131763, <https://doi.org/10.1021/jp9105585>.
- [9] J. S. Smith, O. Isayev, and A. E. Roitberg, *Chem. Sci.* **8**, 3192 (2017).
- [10] J. C. Snyder, M. Rupp, K. Hansen, K.-R. Müller, and K. Burke, *Phys. Rev. Lett.* **108**, 253002 (2012).
- [11] Z. D. Pozun, K. Hansen, D. Sheppard, M. Rupp, K.-R. Müller, and G. Henkelman, *J. Chem. Phys.* **136**, 174101 (2012).
- [12] M. Ceriotti, C. Clementi, and O. Anatole von Lilienfeld, *Chem. Rev.* **121**, 9719 (2021).
- [13] M. Ceriotti, C. Clementi, and O. Anatole von Lilienfeld, *The Journal of Chemical Physics* **154**, 160401 (2021), <https://doi.org/10.1063/5.0051418>.
- [14] O. A. von Lilienfeld, R. Ramakrishnan, M. Rupp, and A. Knoll, *International Journal of Quantum Chemistry* **115**, 1084 (2015), <https://onlinelibrary.wiley.com/doi/pdf/10.1002/qua.24912>.
- [15] L. M. Ghiringhelli, J. Vybiral, S. V. Levchenko, C. Draxl, and M. Scheffler, *Phys. Rev. Lett.* **114**, 105503 (2015).

- [16] F. Musil, A. Grisafi, A. P. Bartók, C. Ortner, G. Csányi, and M. Ceriotti, *Chemical Reviews* **121**, 9759 (2021), pMID: 34310133, <https://doi.org/10.1021/acs.chemrev.1c00021>.
- [17] R. Ramakrishnan and O. A. von Lilienfeld, *CHIMIA* **69**, 182 (2015).
- [18] V. N. Vapnik, *Statistical Learning Theory* (Wiley-Interscience, 1998).
- [19] C. R. Collins, G. J. Gordon, O. A. von Lilienfeld, and D. J. Yaron, *The Journal of Chemical Physics* **148**, 241718 (2018), <https://doi.org/10.1063/1.5020441>.
- [20] J. Behler, *The Journal of Chemical Physics* **134**, 074106 (2011), <https://doi.org/10.1063/1.3553717>.
- [21] L. Zhu, M. Amsler, T. Fuhrer, B. Schaefer, S. Faraji, S. Rostami, S. A. Ghasemi, A. Sadeghi, M. Grauzinyte, C. Wolverton, and S. Goedecker, *The Journal of Chemical Physics* **144**, 034203 (2016), <https://doi.org/10.1063/1.4940026>.
- [22] H. Huo and M. Rupp, *Machine Learning: Science and Technology* **3**, 045017 (2022).
- [23] M. Gastegger, L. Schwiedrzik, M. Bittermann, F. Berzsenyi, and P. Marquetand, *The Journal of Chemical Physics* **148**, 241709 (2018), <https://doi.org/10.1063/1.5019667>.
- [24] R. Drautz, *Phys. Rev. B* **99**, 014104 (2019).
- [25] B. J. Braams and J. M. Bowman, *International Reviews in Physical Chemistry* **28**, 577 (2009), <https://doi.org/10.1080/01442350903234923>.
- [26] M. J. Hirn, N. Poilvert, and S. Mallat, *CoRR abs/1502.02077* (2015), 1502.02077.
- [27] A. V. Shapeev, *Multiscale Modeling & Simulation* **14**, 1153 (2016), <https://doi.org/10.1137/15M1054183>.
- [28] J. Nigam, S. Pozdnyakov, and M. Ceriotti, *The Journal of Chemical Physics* **153**, 121101 (2020), <https://doi.org/10.1063/5.0021116>.
- [29] V. Zaverkin and J. Kästner, *Journal of Chemical Theory and Computation* **16**, 5410 (2020), pMID: 32672968, <https://doi.org/10.1021/acs.jctc.0c00347>.
- [30] R. Jinnouchi, F. Karsai, C. Verdi, R. Asahi, and G. Kresse, *The Journal of Chemical Physics* **152**, 234102 (2020), <https://doi.org/10.1063/5.0009491>.
- [31] A. Thompson, L. Swiler, C. Trott, S. Foiles, and G. Tucker, *Journal of Computational Physics* **285**, 316 (2015).
- [32] M. J. Willatt, F. Musil, and M. Ceriotti, *Phys. Chem. Chem. Phys.* **20**, 29661 (2018).
- [33] M. F. Langer, A. Goëßmann, and M. Rupp, *npj Computational Materials* **8**, 41 (2022).
- [34] A. S. Christensen, L. A. Bratholm, F. A. Faber, and O. Anatole von Lilienfeld, *The Journal of Chemical Physics* **152**, 044107 (2020), <https://doi.org/10.1063/1.5126701>.
- [35] F. A. Faber, A. S. Christensen, B. Huang, and O. A. von Lilienfeld, *The Journal of Chemical Physics* **148**, 241717 (2018), <https://doi.org/10.1063/1.5020710>.
- [36] A. P. Bartók, R. Kondor, and G. Csányi, *Phys. Rev. B* **87**, 184115 (2013).
- [37] B. Huang and O. A. von Lilienfeld, “Quantum machine learning using atom-in-molecule-based fragments selected on-the-fly,” (2017).
- [38] K. Hansen, F. Biegler, R. Ramakrishnan, W. Pronobis, O. A. von Lilienfeld, K.-R. Müller, and A. Tkatchenko, *The Journal of Physical Chemistry Letters* **6**, 2326 (2015), pMID: 26113956, <https://doi.org/10.1021/acs.jpcclett.5b00831>.
- [39] C. E. Rasmussen and C. K. I. Williams, *Gaussian processes for machine learning.*, Adaptive computation and machine learning (MIT Press, 2006) pp. I–XVIII, 1–248.
- [40] S. De, A. P. Bartók, G. Csányi, and M. Ceriotti, *Phys. Chem. Chem. Phys.* **18**, 13754 (2016).
- [41] A. P. Bartók and G. Csányi, *International Journal of Quantum Chemistry* **115**, 1051 (2015).
- [42] S. Chmiela, V. Vassilev-Galindo, O. T. Unke, A. Kabylda, H. E. Saucedo, A. Tkatchenko, and K.-R. Müller, *Science Advances* **9**, eadf0873 (2023), <https://www.science.org/doi/pdf/10.1126/sciadv.adf0873>.
- [43] F. A. Faber, A. Lindmaa, O. A. von Lilienfeld, and R. Armiento, *Phys. Rev. Lett.* **117**, 135502 (2016).
- [44] P. M. Morse, *Phys. Rev.* **34**, 57 (1929).
- [45] J. E. Jones, *Proceedings of the Royal Society of London. Series A* (1924).
- [46] B. M. Axilrod and E. Teller, *The Journal of Chemical Physics* **11**, 299 (1943), <https://doi.org/10.1063/1.1723844>.
- [47] F. H. Stillinger and T. A. Weber, *Phys. Rev. B* **31**, 5262 (1985).
- [48] R. Ramakrishnan, P. O. Dral, M. Rupp, and O. A. von Lilienfeld, *Scientific Data* **1** (2014).
- [49] M. Rupp, A. Tkatchenko, K.-R. Müller, and O. A. von Lilienfeld, *Phys. Rev. Lett.* **108**, 058301 (2012).
- [50] C. Isert, K. Atz, J. Jiménez-Luna, and G. Schneider, *Scientific Data* **9**, 273 (2022).
- [51] S. N. Pozdnyakov, M. J. Willatt, A. P. Bartók, C. Ortner, G. Csányi, and M. Ceriotti, *Phys. Rev. Lett.* **125**, 166001 (2020).
- [52] B. Huang and O. A. von Lilienfeld, *The Journal of Chemical Physics* **145**, 161102 (2016), <https://doi.org/10.1063/1.4964627>.
- [53] E. Parzen, *The Annals of Mathematical Statistics* **33**, 1065 (1962).
- [54] S.-i. Amari and H. Nagaoka, *Methods of information geometry*, Vol. 191 (American Mathematical Soc., 2000).
- [55] M. P. Deisenroth, A. A. Faisal, and C. S. Ong, *Mathematics for Machine Learning* (Cambridge University Press, 2020).
- [56] K. T. Schütt, S. Chmiela, O. A. von Lilienfeld, A. Tkatchenko, K. Tsuda, and K.-R. Müller, *Machine Learning Meets Quantum Physics* (Springer, 2020).
- [57] O. Çaylak, O. A. von Lilienfeld, and B. Baumeier, *Machine Learning: Science and Technology* **1**, 03LT01 (2020).
- [58] R. Fabregat, P. van Gerwen, M. Haeberle, F. Eisenbrand, and C. Corminboeuf, *Machine Learning: Science and Technology* **3**, 035015 (2022).
- [59] C. Cortes, L. D. Jackel, S. A. Solla, V. Vapnik, and J. S. Denker, in *Advances in Neural Information Processing Systems* (1994) pp. 327–334.
- [60] K. R. Müller, M. Finke, N. Murata, K. Schulten, and S. Amari, *Neural Comp.* **8**, 1085 (1996).
- [61] T. Head, M. Kumar, H. Nahrstaedt, G. Louppe, and I. Shcherbatyi, “scikit-optimize/scikit-optimize,” (2021).
- [62] D. C. Liu and J. Nocedal, *Mathematical Programming* **45**, 503 (1989).
- [63] C. R. Harris, K. J. Millman, S. J. van der Walt, R. Gommers, P. Virtanen, D. Cournapeau, E. Wieser, J. Taylor, S. Berg, N. J. Smith, R. Kern, M. Picus, S. Hoyer, M. H. van Kerkwijk, M. Brett, A. Haldane, J. F. del Río, M. Wiebe, P. Peterson, P. Gérard-Marchant, K. Shep-

- pard, T. Reddy, W. Weckesser, H. Abbasi, C. Gohlke, and T. E. Oliphant, *Nature* **585**, 357 (2020).
- [64] S. K. Lam, A. Pitrou, and S. Seibert, in *Proceedings of the Second Workshop on the LLVM Compiler Infrastructure in HPC*, LLVM '15 (Association for Computing Machinery, New York, NY, USA, 2015).
- [65] A. D. Becke, *The Journal of Chemical Physics* **98**, 5648 (1993), <https://doi.org/10.1063/1.464913>.
- [66] C. Lee, W. Yang, and R. G. Parr, *Phys. Rev. B* **37**, 785 (1988).
- [67] G. A. Petersson, A. Bennett, T. G. Tensfeldt, M. A. Al-Laham, W. A. Shirley, and J. Mantzaris, *The Journal of Chemical Physics* **89**, 2193 (1988), <https://doi.org/10.1063/1.455064>.
- [68] J.-D. Chai and M. Head-Gordon, *Phys. Chem. Chem. Phys.* **10**, 6615 (2008).
- [69] F. Weigend and R. Ahlrichs, *Phys. Chem. Chem. Phys.* **7**, 3297 (2005).
- [70] K. Yao, J. E. Herr, D. W. Toth, R. Mckintyre, and J. Parkhill, *Chemical Science* **9**, 2261 (2018).
- [71] A. S. Christensen, L. A. Bratholm, F. A. Faber, B. Huang, A. Tkatchenko, K. R. Müller, and O. A. von Lilienfeld, “Qml: A python toolkit for quantum machine learning,” (2017).
- [72] L. Himanen, M. O. J. Jäger, E. V. Morooka, F. Federici Canova, Y. S. Ranawat, D. Z. Gao, P. Rinke, and A. S. Foster, *Computer Physics Communications* **247**, 106949 (2020).
- [73] M. Rupp, *International Journal of Quantum Chemistry* **115**, 1058 (2015).
- [74] K. T. Schütt, P. Kessel, M. Gastegger, K. A. Nicoli, A. Tkatchenko, and K.-R. Müller, *Journal of Chemical Theory and Computation* **15**, 448 (2018).
- [75] K. T. Schütt, O. T. Unke, and M. Gastegger, *CoRR abs/2102.03150* (2021), 2102.03150.
- [76] K. Schütt, P.-J. Kindermans, H. E. Saucedo Felix, S. Chmiela, A. Tkatchenko, and K.-R. Müller, in *Advances in Neural Information Processing Systems*, Vol. 30, edited by I. Guyon, U. V. Luxburg, S. Bengio, H. Wallach, R. Fergus, S. Vishwanathan, and R. Garnett (Curran Associates, Inc., 2017).
- [77] A. Musaelian, S. Batzner, A. Johansson, L. Sun, C. J. Owen, M. Kornbluth, and B. Kozinsky, *Nature Communications* **14** (2023), [10.1038/s41467-023-36329-y](https://doi.org/10.1038/s41467-023-36329-y).
- [78] S. Batzner, A. Musaelian, L. Sun, M. Geiger, J. P. Mailoa, M. Kornbluth, N. Molinari, T. E. Smidt, and B. Kozinsky, *Nature Communications* **13** (2022), [10.1038/s41467-022-29939-5](https://doi.org/10.1038/s41467-022-29939-5).
- [79] M. Geiger, T. Smidt, M. Alby, B. K. Miller, W. Boomsma, B. Dice, K. Lapchevskiy, M. Weiler, Michał Tyszkiewicz, M. Uhrin, S. Batzner, D. Madisetti, J. Frellsen, N. Jung, S. Sanborn, Jkh, Mingjian Wen, J. Rackers, M. Rød, and M. Bailey, “e3nn/e3nn: 2022-12-12,” (2022).
- [80] M. Geiger, T. Smidt, A. M., B. K. Miller, W. Boomsma, B. Dice, K. Lapchevskiy, M. Weiler, M. Tyszkiewicz, S. Batzner, D. Madisetti, M. Uhrin, J. Frellsen, N. Jung, S. Sanborn, M. Wen, J. Rackers, M. Rød, and M. Bailey, “Euclidean neural networks: e3nn,” (2022).
- [81] M. Geiger and T. Smidt, “e3nn: Euclidean neural networks,” (2022).
- [82] J. Townsend, C. P. Micucci, J. H. Hymel, V. Maroulas, and K. D. Vogiatzis, *Nature Communications* **11**, 3230 (2020).
- [83] F. Bigi, S. N. Pozdnyakov, and M. Ceriotti, “Wigner kernels: body-ordered equivariant machine learning without a basis,” (2023), [arXiv:2303.04124 \[physics.chem-ph\]](https://arxiv.org/abs/2303.04124).
- [84] N. J. Browning, F. A. Faber, and O. Anatole von Lilienfeld, *The Journal of Chemical Physics* **157**, 214801 (2022).
- [85] K. Atz, C. Isert, M. N. Böcker, J. Jiménez-Luna, and G. Schneider, *Physical Chemistry Chemical Physics* **24**, 10775 (2022).
- [86] C. Bannwarth, S. Ehlert, and S. Grimme, *Journal of Chemical Theory and Computation* **15**, 1652 (2019).
- [87] G. Montavon, M. Rupp, V. Gobre, A. Vazquez-Mayagoitia, K. Hansen, A. Tkatchenko, K.-R. Müller, and O. A. von Lilienfeld, *New Journal of Physics* **15**, 095003 (2013).
- [88] L. C. Blum and J.-L. Raymond, *J. Am. Chem. Soc.* **131**, 8732 (2009).
- [89] A. S. Christensen and O. A. von Lilienfeld, *Machine Learning: Science and Technology* **1**, 045018 (2020).
- [90] A. S. Christensen and A. V. lilienfeld, (2020), [10.6084/m9.figshare.12672038.v3](https://arxiv.org/abs/2006.08084).
- [91] S. Chmiela, A. Tkatchenko, H. E. Saucedo, I. Poltavsky, K. T. Schütt, and K.-R. Müller, *Science Advances* **3** (2017), [10.1126/sciadv.1603015](https://doi.org/10.1126/sciadv.1603015).
- [92] S. Chmiela, H. E. Saucedo, K.-R. Müller, and A. Tkatchenko, *Nature Communications* **9** (2018), [10.1038/s41467-018-06169-2](https://doi.org/10.1038/s41467-018-06169-2).
- [93] A. S. Christensen, F. A. Faber, and O. A. von Lilienfeld, *The Journal of Chemical Physics* **150**, 064105 (2019), <https://doi.org/10.1063/1.5053562>.